HORIBA Scientific

JOBIN YVON Technology

Raman Spectroscopy

Three Dimensional Raman Imaging

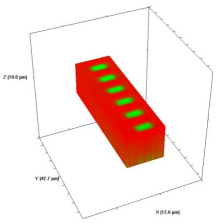

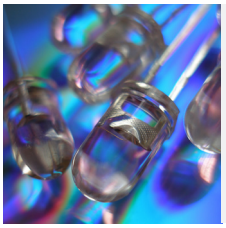

Application Note

Optoelectronic RA68

David Tuschel, Manager of Raman Applications, HORIBA Instruments Incorporated, 3880 Park Avenue Edison, New Jersey, USA 08820

Abstract

Segmented channel waveguides have been fabricated in single crystal $KTiOPO_4$ through a topotactic process of partial cation exchange. The ion-exchanged waveguides maintain the high nonlinear susceptibility of $KTiOPO_4$ to function as frequency doubling laser light sources. We apply three dimensional (3D) Raman imaging to understand and characterize the changes to the chemical bonding and crystalline structure as well as measure the volumetric structure of the waveguide segments.

Keywords: 3D Raman Imaging, Waveguides, Nonlinear materials

Fabrication of Waveguides

The ion-exchange process is a convenient method for the fabrication of channel waveguides in crystals with high nonlinear susceptibility and electro-optic coefficients. The idea is to create a channel in which the refractive index has been sufficiently changed to achieve laser beam confinement (wave guiding) while retaining the high nonlinear optical susceptibility of the host crystal. Through either quasi-phase matching in continuous waveguides or balanced phase matching in segmented waveguides, second harmonic generation can be achieved to produce short wavelength laser output from an end fired near infrared laser beam. The waveguides are generated through a topotactic chemical reaction in which a nonlinear single crystal such as $LiNbO_3$ or $KTiOPO_4$ is exposed to an acid or salt melt with a cation different from that of the host crystal. For example, if a single crystal of $KTiOPO_4$ is exposed to $RbNO_3$ at elevated temperature over a select period of time, a cation exchange will occur forming $Rb_xK_{1-x}TiOPO_4$ in a certain volume near the surface of the crystal. Waveguides fabricated in this fashion have a technological function as frequency doubled waveguide lasers, electro-optic shifters, and Mach-Zehnder interferometric devices.

The waveguides are fabricated by depositing a metal coating on the Z-face of the crystal and subsequently using photolithographic techniques to create a pattern of openings in the metal. The open areas are exposed for ion exchange to form the waveguides and optical circuitry. A typical process exposes the $KTiOPO_4$ surface to $RbNO_3$ at elevated temperatures; e.g., (350°C) for 20 minutes (1).

The temperature and particularly the duration of the ion exchange process affect the final volumetric structure of the waveguides.

Raman Spectroscopy of Rb-Exchanged $KTiOPO_4$

To understand the spectral changes observed in the Rb^+-exchanged regions of $KTiOPO_4$ (R/KTP) we need to first consider the Raman spectra of single crystals of $KTiOPO_4$ (KTP), and $RbTiOPO_4$ (RTP). The spectra of the single crystals and the ion-exchanged waveguides are highly dependent upon the crystal orientation relative to the direction of the incident laser beam and polarization. Raman spectra of single crystals of $KTiOPO_4$ and $RbTiOPO_4$ are shown in Figure 1.

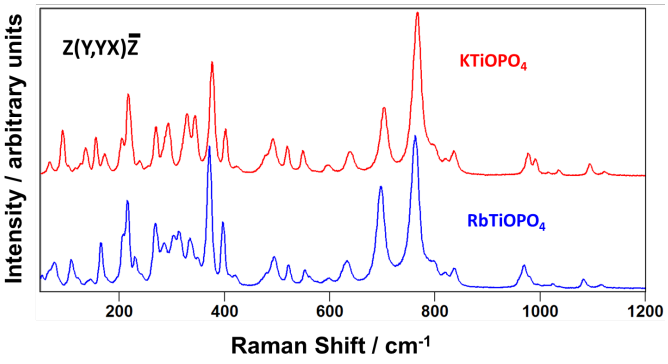

Figure 1: Raman spectra of $KTiOPO_4$ and $RbTiOPO_4$ single crystals.

The inset Porto notation indicates that the laser beam propagated along the Z-axis incident upon the Z-face of the crystal with polarization along the Y-axis and backscattered light was collected without the use of a polarization analyzer (YX). The $KTiOPO_4$ and $RbTiOPO_4$ spectra are similar because the Raman scattering from both crystals arises primarily from the octahedral TiO_6 and tetrahedral PO_4 structural units. The greater differences appear at Raman shifts less than 375 cm^{-1} where the neighboring cation has a more significant effect on the vibrational bending motions of the TiO_6 and PO_4 groups.

These $KTiOPO_4$ and $RbTiOPO_4$ spectra would normally represent our spectral limits as we analyze compounds with varying stoichiometries of $K_{1-x}Rb_xTiOPO_4$ prepared from a melt. However, remember that our waveguides are prepared by a topotactic chemical reaction in which the host crystal, which is built for the K^+ ion, exchanges some of the cations for the Rb^+ ion. Therefore, we have an entirely different structure than one that would be formed from a mixed stoichiometric composition generated from the melt in which the most energetically favorable bond lengths, bond angles and lattice spacings would be established for the specific $K_{1-x}Rb_xTiOPO_4$ composition. Here you have the Rb^+ ion with a much larger atomic radius (r = 1.49 Å) replacing K^+ (r = 1.33 Å) in a crystal "built" for the smaller K^+ cation. You can appreciate the importance of this difference by viewing the Ti coordination environment of $KTiOPO_4$ shown in Figure 2.

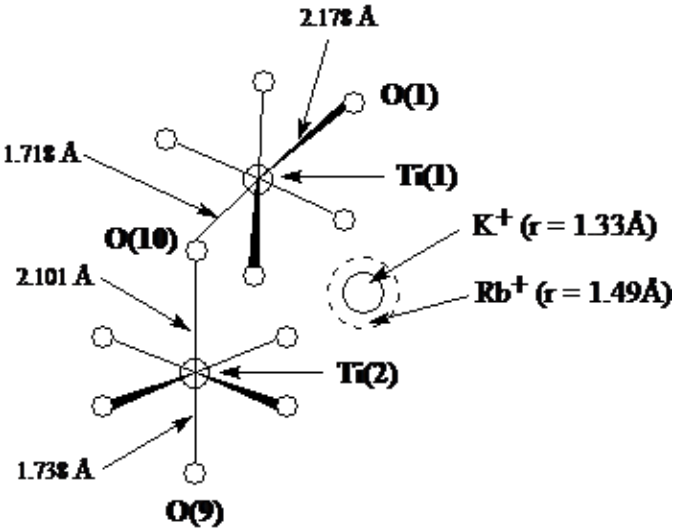

Figure 2: Ti coordination environment in $KTiOPO_4$.

The exchange of K^+ for Rb^+ increases the chemical interaction of the TiO_6 species with the larger Rb^+ cation, induces strain in the crystal lattice, and forces a change in the solid state structure to reduce the energy. These changes in chemical bonding and solid state structure are the origin of the local change in refractive index to form a waveguide.

We wish to generate 3D Raman images along the waveguide; therefore, we need to map the Z-face with the incident laser beam parallel to the Z-axis. Raman spectra of a region of R/KTP and KTP adjacent to it are shown in Figure 3.

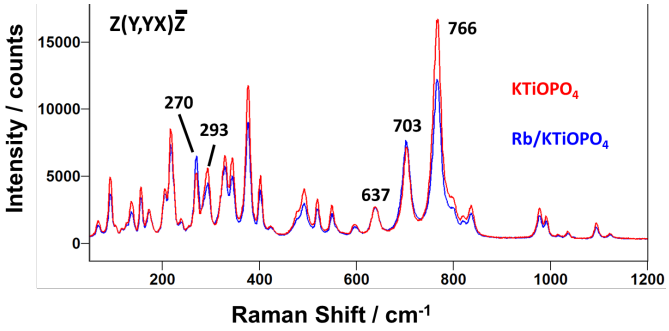

Figure 3: Raman spectra of a Rb^+-exchanged $KTiOPO_4$ region and the $KTiOPO_4$ adjacent to it.

These spectra are plotted in absolute counts and are not normalized. The Raman band at 637 cm^{-1} is significant insofar as it has the same signal strength for R/KTP and the adjacent KTP. Therefore, any differences in the absolute strengths of the other bands indicate varying differences in relative strengths between R/KTP and KTP Raman bands, thereby allowing an easy distinction of the two compositions. In particular, note the reversal in 270 and 293 cm^{-1} relative band strength in transforming KTP to R/KTP. Consequently, the application of direct classical least squares analysis to the hyperspectral data set acquired by mapping in either 2 or 3 dimensions produces Raman images of the waveguides and host crystal based upon their distinct Raman signatures arising from changes in chemical bonding and solid state structure. All Raman images shown here were generated by direct classical least squares analyses in supervised mode, i.e., target image spectra were fit with acquired reference spectra of KTP and R/KTP.

3D Raman Imaging of Segmented Waveguides

We applied three dimensional (3D) Raman imaging to understand and characterize changes to the chemical bonding and solid state structure as well as measure the volumetric structure of the waveguide segments. A 3D Raman image of a portion of a segmented waveguide is shown in Figure 4. The hyperspectral data that form the basis of the image were acquired in 0.2 µm XY increments with axial spacings of 2 µm from the surface to a final translation stage position of -10 µm. The dimensions that appear on the box framing the image in Figure 4 (and all subsequent volumetric Raman images) correspond to the dimensions of the full image within the box.

Thus, you see a segmented channel waveguide imaged over 42.7 µm (Y-axis) by 12.6 µm (X-axis) over a stage travel depth of 10 µm. We note here that the depth dimensions reported and shown in the images are actually of axial stage position only. The axial stage positions do not correspond precisely to the actual focal depth of the laser beam in the material. To obtain truly quantitative confocal images, one must take into account the effect of the material's refractive index on the laser beam focus. To do that, we refer readers to the indispensable work on this subject by Neil Everall (2-6).

3D Raman imaging is best suited for a real time display during which one can slice through the voxels to uncover the planar images hidden within that reveal spatially varying changes in chemical composition, bonding and solid state structure. Restricted to the presentation in print form, we opt for showing a volumetric image with a portion sliced away to reveal the structure within. Figure 5 shows the volumetric image of Figure 4 with approximately one-half of the X-axis portion of the original 3D image sliced off to expose the depth of the Rb^+-exchanged waveguide segments. The most striking aspect revealed by the 3D imaging is how the exchange occurs so deeply and uniformly along the crystallographic Z-axis. There is almost no lateral mass transport of Rb^+. This is quite contrary to the radial diffusion that one might have expected, similar to that observed when placing a drop of a colored fluid in another that is transparent. Furthermore, we can see in this image the degree of Rb^+ exchange is beginning to diminish only near a depth of 10 µm.

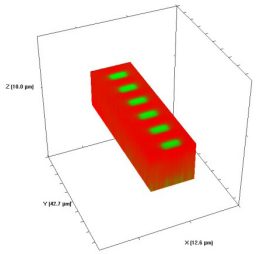

Figure 4: 3D Raman image of a portion of a segmented Rb^+-exchanged $KTiOPO_4$ waveguide device fabricated by exposing open surfaces to molten $RbNO_3$ for 20 min.

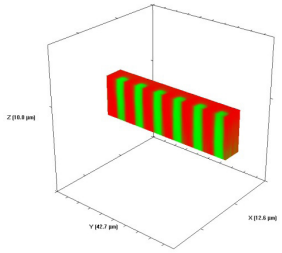

Figure 5: Sliced portion of the 3D Raman image of the waveguide shown in Fig. 4.

Turning now to a deeper analysis of the segmented waveguides, the 3D image of the full volume X (8.3 µm), Y (6.2 µm) and Z (14.0 µm) Rb^+-exchanged segment is shown in Figure 6. The Raman hyperspectral data set was acquired by translating the sample in 0.2 µm X and Y increments and 1.0 µm increments along the Z-axis.

This is a 5 µm wide Rb^+-exchanged segment and over a depth of 14 µm there is no indication of lateral transport of the Rb^+ ions in the XY-plane to the borders or outer surfaces of the 3D image. Rotating the full volumetric image, adjusting the transparency of the two components, and slicing off planes of the volumetric data set is the ideal way of analyzing a 3D Raman image. However, restricted as we are to the print page a look at volumetric fractions will have to suffice. Figure 7 shows the same volumetric data set but with one-half of the Y-axis sliced off to reveal the 3D structure of one 5 µm Rb^+-exchanged segment. We see that the axial boundaries are indeed vertical with the Rb^+ exchange tapering off at a depth of approximately 10 µm.

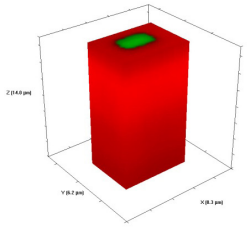

Figure 6: 3D Raman image of one segment of a Rb^+-exchanged KTiOPO4 waveguide exposed to molten $RbNO_3$ for 20 min.

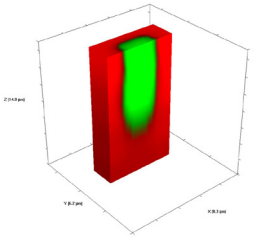

Figure 7: Sliced portion of the 3D Raman image of one segment of a Rb^+-exchanged $KTiOPO_4$ exposed to molten $RbNO_3$ for 20 min shown in Fig 6.

A reasonable question is whether a smaller size of the opening in the metal mask would affect the lateral mass transport and therefore the depth aspect ratio of the waveguide segments. We have seen that the 5 µm R/KTP segments have depths of approximately 10 µm. The smallest segment width of the waveguide device is 3 µm. A Raman hyperspectral data set of the 3 µm Rb^+-exchanged segmented waveguide was acquired by translating the sample in 0.5 µm X and Y increments and 1.0 µm increments along the Z-axis. The 3D image of the full volume X (8.2 µm), Y (13.5 µm) and Z (10.0 µm) is shown in Figure 8.

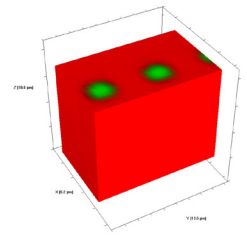

Figure 8: 3D Raman image of a portion of a segmented Rb^+-exchanged $KTiOPO_4$ waveguide exposed to molten $RbNO_3$ for 20 min.

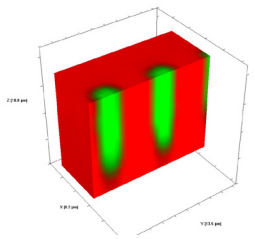

Figure 9: Sliced portion of the 3D Raman image of a segmented Rb^+-exchanged $KTiOPO_4$ waveguide exposed to molten $RbNO_3$ for 20 min shown in Fig 8.

Again we see no evidence of lateral mass transport of Rb^+ exchange over a depth of 10 µm to the outer border or surface of the full volumetric image. Slicing away a portion of the X-axis and the Y-axis exposes the volumetric structure of the waveguide segments as seen in Figures 9 and 10, respectively. Even for the small 3 µm Rb^+ exchanged segments the mass transport occurs strictly along the crystallographic Z-axis with no evidence of lateral mass transport of Rb^+ exchange in the crystallographic XY-plane.

The important conclusion from these Raman images with respect to the fabrication of Rb^+-exchanged $KTiOPO_4$ waveguides is that the pattern and sizes of the openings in the mask on the crystal face will be retained axially as mass transport of Rb^+ exchange occurs almost exclusively along the crystallographic Z axis of $KTiOPO_4$.

Conclusion

We have applied 3D Raman imaging to understand and characterize the changes to the chemical bonding and crystalline structure as well as measure the volumetric structure of the waveguides formed through topotactic chemical reactions. Raman images of Rb^+-exchanged $KTiOPO_4$ waveguides reveal that the pattern and sizes of the openings in the mask created by photolithographic processes on the crystal Z-face will be retained axially as mass transport of Rb^+ exchange occurs almost exclusively along the crystallographic Z-axis of $KTiOPO_4$.

References

(1) D.D. Tuschel, G.R. Paz-Pujalt and W.P. Risk, Appl. Phys. Lett. 66, 1035-1037 (1995).
(2) N.J. Everall, Appl. Spec. 54, 773-782 (2000).
(3) N.J. Everall, Appl. Spec. 54, 1515-1520 (2000).
(4) N.J. Everall, J. Raman Spec. 45, 133-138 (2014).
(5) N.J. Everall, Spectroscopy 19(10) 22-27 (2004).
(6) N.J. Everall, Spectroscopy 19(11) 16-25 (2004).

JOBIN YVON Technology

HORIBA Scientific

info.sci@horiba.com www.horiba.com/scientific

USA: +1 732 494 8660
UK: +44 (0)20 8204 8142
China: +86 (0)21 6289 6060
France: +33 (0)1 69 74 72 00
Italy: +39 2 5760 3050
Brazil: +55 (0)11 2923 5400
Germany: +49 (0)6251 8475 -0
Japan: +81 (75) 313 8123
Other: +33 (0)1 69 74 72 00